

Chapter 1

Introduction

From the Vedas to the ancient Greeks, generations have described the constituents of nature in terms of indivisible ‘elements’. It wasn’t until the beginning of the 20th century that the ancient elements of earth, wind, fire, water, and the aether were abandoned for the atomic theory of nature. By the 1960’s, what would become known as the Standard Model of Particle Physics was taking shape. The five ancient elements were replaced by the fundamental particles: quarks and leptons comprising the spin 1/2 fermions and the force carrying bosons with spin 1 as seen in Fig. 1.1

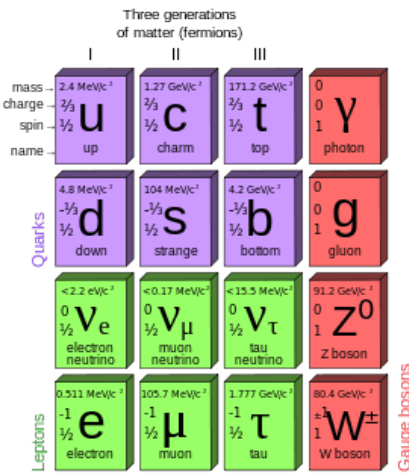


Figure 1.1: The fundamental particles of the Standard Model[1].

The Standard Model is the unification of the three symmetry groups, $SU(3) \times SU(2) \times U(1)$, representing the strong, weak, and electromagnetic forces[2]. In terms of scientific

accomplishments the Standard Model is one of the most tested theories of nature with an agreement between the theory and observed results up to ten digits[3].

Even though the Standard Model gives us a deep understanding for many natural phenomena and has a wide range of uses; understanding the evolution of the Big Bang, how atoms and molecules bond, the nature of light, to cancer treatments and nuclear security it is fundamentally an incomplete theory of nature. The fact that Gravity has yet to be unified into a quantum theory tells us that the Standard Model is incomplete. High energy experiments give us some of the most extreme conditions possible to test the Standard Model and to look for phenomena outside of the theory. Are their new symmetries and laws that manifest at high energies? Can we create dark matter or dark energy in a laboratory? Are quarks and leptons fundamental or finite in size? Do the four fundamental forces emerge from some yet unknown unified force? And why is antimatter absent in the Universe? All of these open questions are of great interest and currently form large areas of active research.

The theory of strong interactions, Quantum Chromodynamics(QCD), is described by the SU(3) group and similar in analogy to the electric charge of Quantum Electrodynamics (QED) carries color charge, red, green, and blue. Quarks and gluons are colloquially known as partons and are particles that interact via the strong force. At low energies and over large length scales partons are confined to a color neutral state and these particles must clump together into color neutral hadrons. As two colored partons began to separate, at some point it becomes energetically favorable to create a quark–antiquark pair out of the vacuum rather than expanding the distance between neighboring partons. Due to confinement, quark interactions at high energy collider experiments manifest themselves as a spray of hadrons known as a ‘jet’. The other main attribute of QCD is asymptotic freedom, as the interactions between partons becomes more energetic and the length scale decreases the strong coupling constant becomes exceedingly small, $\alpha_{strong} \ll 1$, and the partons freely interact with one another. Due to asymptotic freedom nuclear matter undergoes a phase transition called the Quark–Gluon Plasma (QGP) at high energies and densities

This thesis will present an overview of Quantum Chromodynamics in Chapter 2, with an emphasis on jet physics and heavy ion collisions. Chapter 3 will give a brief overview of the Large Hadron Collider and the ALICE experiment, including the relevant subsystems

for this jet analysis. Jet results from the ALICE detector along with comparissons to QCD simulations with systematic uncertainty calculations and unfolding for detector effects will be given in Chapter 4. The ALICE time projection chamber will be upgraded to a continous readout mode, the physics motivation behind this and author's contributions will be discussed in Chapter 5. Chapter 6 will serve as a final discussion, outlook, and conclusion.

Chapter 2

Quantum Chromodynamics

In 1968 deep inelastic scatterings performed at the Stanford Linear Accelerator Center showed that the proton had internal structure[4] called partons at the time. Within a decade of this discovery the partons were broken into two categories: the mass carrying fermions were known as the quarks and the gauge boson force carriers were called gluons. The interactions of these two types of particles were described by the quantum field theory known as quantum chromodynamics (QCD) and by the SU(3) symmetry group. SU(3) guarantees that color charge is conserved and this results in quarks grouping together into ‘colorless’ hadrons.

2.1 The QCD Lagrangian

QCD is the strongest of the known fundamental forces. It is a gauge field theory described by the Lagrangian density

$$\mathcal{L} = -\frac{1}{4}F_{\mu\nu}^\alpha F_{\alpha}^{\mu\nu} - \alpha_s(\bar{q}_j \gamma^\mu T_\alpha q_j)G_\alpha^\mu + \bar{q}_j(i\gamma^\mu \partial_\mu - m)q_j \quad (2.1)$$

where q and \bar{q} represent the color anti-color fields summed over color j , α_s is the strong coupling strength, γ^μ is the Dirac gamma matrix, G_α^μ is the gauge field for color α , is similar in analogy to the \mathbf{W} matrix from the electroweak theory. $F_{\mu\nu}^\alpha$ is the field strength tensor and it describes the gluon interactions. The first term of the Lagrangian is the gluon contribution

and carries no mass term. The second term of the Lagrangian describes how quarks and gluons interact with each other. The final term describes quark interactions and the coupling between them and will be explored further in this thesis.

At short distances, less than 0.2 fm , the strong coupling constant becomes exceedingly small and second term of the Lagrangian displays an important property known as asymptotic freedom[5].

$$\alpha_s = \frac{1}{\beta_0 \ln(Q^2/\Lambda^2)} \quad (2.2)$$

where α_s is the strong coupling constant, Q^2 is the momentum transfer between two interacting partons, and Λ^2 is a cutoff below which QCD phenomena are strongly suppressed and β_0 is a correction factor.

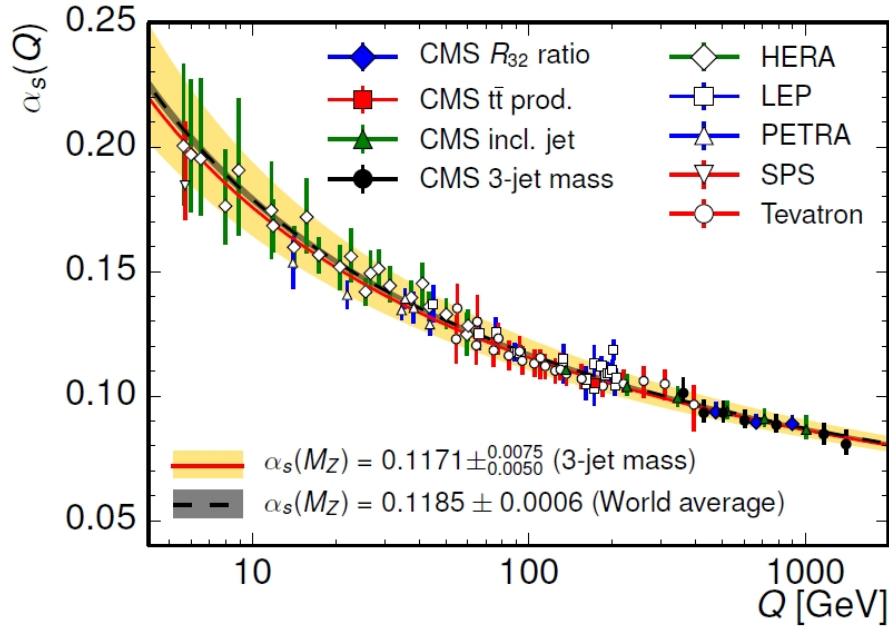


Figure 2.1: Strong coupling constant (α_s) as a function of the momentum transfer (Q)[6].

2.2 Jets

Hard probes (large Q^2 interactions), are produced in the earliest stages of a high energy collision when the largest momentum transfer processes occur. As two highly energetic

partons propagate away from one another, in a back-to-back fashion, they will instigate a shower of daughter partons via gluon radiation and the generation of low-mass $q\bar{q}$ pairs. The clustering of these daughter partons together is colloquially known as a ‘jet’. The physicist James Daniel Bjorken postulated that a correlation could be surmised by summing over the final state transverse momentum of the daughter partons that form a jet to the parton that initiated the hard scattering[7][8]. This has lead to jets becoming the work-horse for both experimentalists and theoreticians over the past 30 years in probing QCD phenomena. This thesis makes use of jets as an important probe of QCD and the following sections are devoted to developing a background for both the theoretical and experimental treatment of jet physics.

2.2.1 Jet Production and the Factorization Theorem

Due to confinement bare quarks are unobserved, therefore experimentalists must probe QCD interactions by detecting the color neutral final state hadrons measured in collider experiments. Fortunately, the factorization theorem (Equation 2.3) allows for the final state jet cross section to be broken into a number of steps that can either be calculated perturbatively using pQCD or modeled phenomenologically. Using the factorization theorem the jet cross section in a pp collision is,

$$d\sigma^{pp \rightarrow jet} \sim f_{a/A}(x_1, Q^2) \otimes f_{b/B}(x_2, Q^2) \otimes d\sigma_{ab \rightarrow c+X}(x_1, x_2) \otimes D_{c \rightarrow h/jet}(z, Q^2) \quad (2.3)$$

- $f_{a/A}(x_1, Q^2)$ and $f_{b/B}(x_2, Q^2)$ are the parton distribution functions (PDF) that describe the probability of finding parton, a or b , within nuclei, A and B , with a given momentum fraction, $x \equiv p_{parton}/p_{hadron}$ as a function of Q^2 .
- $d\sigma_{ab \rightarrow c+X}(x_1, x_2)$ is the pQCD parton-parton cross section due to the hard scattering of the two partons, a and b , to an intermediate parton (c).

- $D_{c \rightarrow h/jet}(z, Q^2)$ is the fragmentation function (FF) that describes the probability the an outgoing parton, c , fragments and hadronizes into a final state hadron, h , within a jet with momentum fraction, $z \equiv p_{hadron}/p_{jet}$.

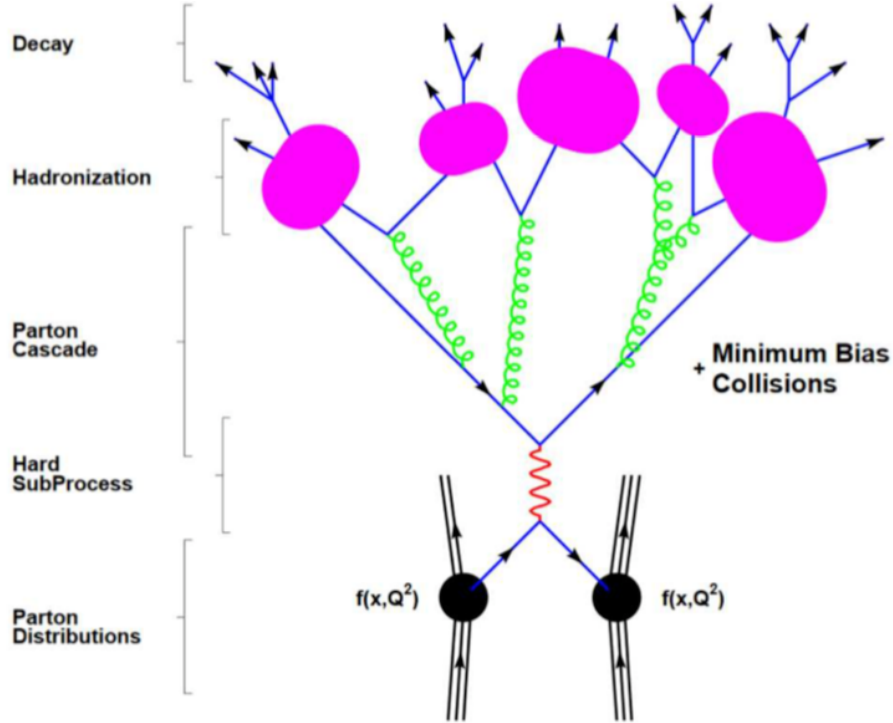


Figure 2.2: Timeline of a proton-proton collision. Starting from the bottom, two partons confined within the colliding protons have a hard interaction. The outgoing partons will induce partonic showers by radiating quarks and gluons. The partonic showers will eventually form into final state hadrons due to confinement which are measured in high energy experiments[9].

Figure 2.2 shows a timeline of a pp collision broken into the relevant steps in accordance to the factorization theorem. One of the best places to fundamentally test QCD phenomena using hard probes, such as jets, are with high energy hadron colliders such as those found at CERN¹, Fermilab, and BNL. The time scale that a hard probe is created in a high energy collision is on the order of $\tau \approx 1/p_T \approx 0.1 \text{ fm}/c$ which probes the initial state these interactions. The factorization theorem allows for a high level of agreement between the QCD theory of nature and experimental observables, but to ascertain this connection we should discuss each term of the factorization theorem in more depth.

¹Discussed in detail in Chapter 3

Parton Distribution Functions

The PDF occurs twice in Equation 2.3 due to the two partons that will undergo the hard scattering being confined in two different protons. PDFs may be thought of as conveying the structure of a nucleon in terms of the number of flavored quarks or gluons ($u(x)$, $d(x)$, $s(x)$, $\bar{u}(x)$, $\bar{d}(x)$, $\bar{s}(x)$, $g(x)$) and must obey certain constraints and summation rules. In the case of a proton, with electric charge ($e = +1$),

$$+1 = \frac{2}{3} \int_0^1 [u(x) - \bar{u}(x)] dx - \frac{1}{3} \int_0^1 [d(x) - \bar{d}(x)] dx \quad (2.4)$$

and isospin ($I = 1/2$),

$$\frac{1}{2} = \frac{1}{2} \int_0^1 [u(x) - \bar{u}(x)] dx - \frac{1}{2} \int_0^1 [d(x) - \bar{d}(x)] dx \quad (2.5)$$

have a solution,

$$\int_0^1 [u(x) - \bar{u}(x)] = 2 \quad (2.6)$$

$$\int_0^1 [d(x) - \bar{d}(x)] dx = 1 \quad (2.7)$$

This corresponds to the classical partonic view that protons contained two up quarks and a down quark, similarly the neutron, with charge $e = 0$ and isospin $I = -1/2$, can be shown that it compromises two down quarks and a up quark. Naively, we could assume that the three quarks composing a proton would each carry a momentum fraction of approximately $1/3$ the total momentum of a proton. However, high energy deep inelastic scattering experiments conducted at the Stanford Linear Collider in the 1960's[10] measured the momentum carried by the three quarks only accounting for about $1/2$ the total proton momentum. This lead to a more complex and dynamic model of the proton structure with the other half of the proton momentum being occupied by neutral partons which would eventually become known as gluons.

Measuring the structure of the partons making up a nucleon is a major endeavor by both theoreticians and experimentalists. Two of the most popular PDFs available to physicists are the CTEQ[12] (Coordinated Theoretical-Experimental Project on QCD) and the NNPDF[13]

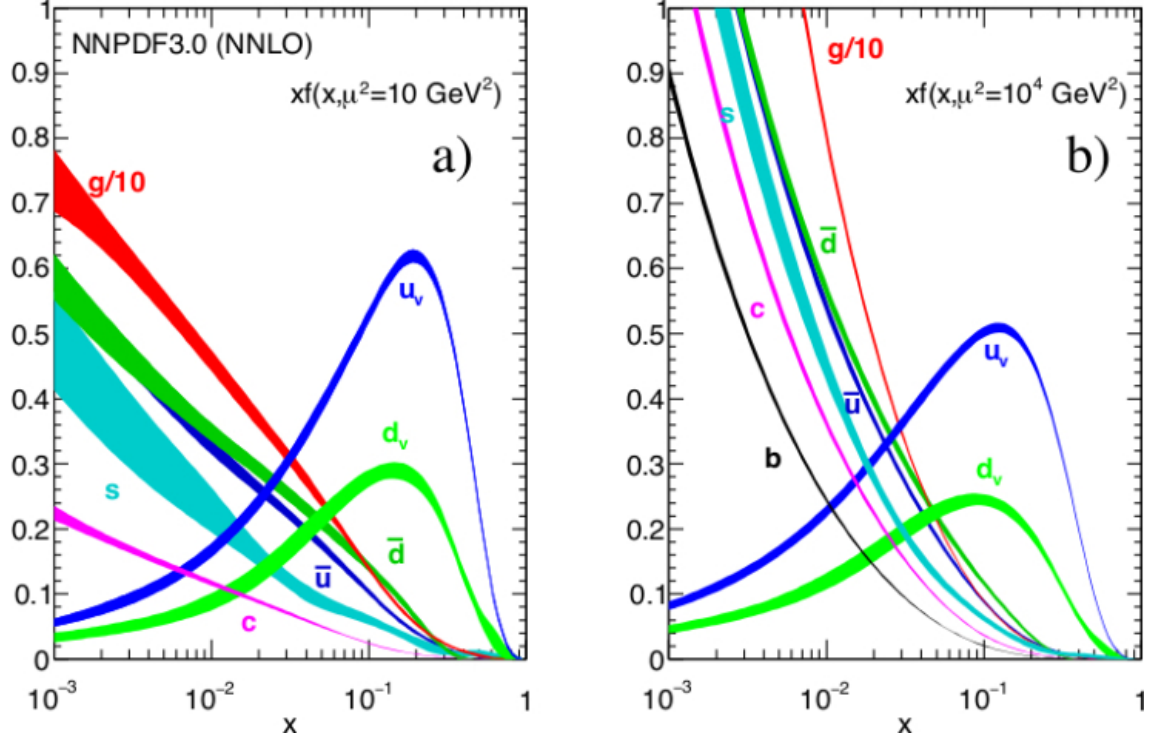


Figure 2.3: Proton PDF at $Q^2 = 10 \text{ GeV}$ (left) and $Q^2 = 10 \text{ TeV}$ (right) from the NNPDF Collaboration[11].

(Neural Network Parton Distribution Function) sets. Figure 2.3 shows the proton PDF as a function of the momentum fraction for two energy ranges, at high values of x the two up quarks account for about 2/3 of the momentum fraction while down quark accounts for about 1/3 the total momentum, these quarks are collectively called the valence quarks. At high energies, low values of x , we see that the proton has non negligible contributions from gluons, anti-quarks, strange, and even charm quarks, these are collectively known as the sea partons. Today, the modern picture of a protons structure is that it is mostly composed of gluons and sea quarks at low values of x and this domination only increases as a function of Q^2 [14].

Parton-Parton Cross-Section

The parton-parton cross section can be calculated using perturbation theory. To the zeroth order in α_s this cross-section would be a simple quark-antiquark annihilation and would be calculable using Feynman diagrams as seen in Figure 2.4[15]. Higher ordered contributions,

such as the creation of virtual gluons, require the hard cross-section to be expanded as a series in terms of α_s . Calculations of the hard cross section that incorporate these higher order terms are known as *next-to-leading order* (NLO) with N denoting the number of terms after the leading order that have been included in the cross-section calculation. Various calculations of the hard cross-section of different QCD processes have been performed over the years typically using either power series or logarithmic expansions of α_s [16] and corrections for LO, NLO, and even NNLO constitutes a very active field in high energy physics.

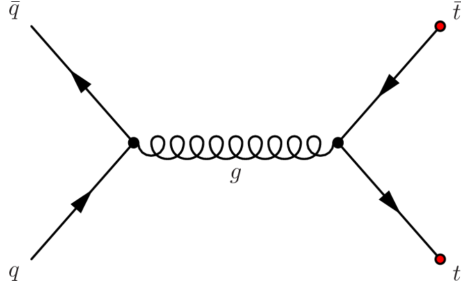


Figure 2.4: Lowest order quark-antiquark annihilation to top-antitop pair[17].

Perturbative techniques of the hard cross-section have been extremely successfully in describing jet features in hadronic collisions[14].

Hadronization

Hadronization is the process by which the colored pQCD partons of form into colorless non-pQCD hadrons and represents a significant barrier in progressing jet physics. This is due to the fact that hadronization encompass several smaller processes which in themselves are hard to characterize. Thus, like PDFs, an accurate description of hadronization requires a phenomenological approach by which experimental results help complement theoretical calculations. Jet production via hadronization[18] follows two distinct stages. First, the partons that underwent a hard scattering start to emit radiation via gluon bremsstrahlung up until time, $t < Q^2$, this is known as the parton cascade. The parton cascade is the precursor of what will become a jet as most of the radiation generated will travel in the same direction as the initial hard scattered parton. However, this immediately poses an issue in jet physics as radiation generated at a wide angle away from the momentum axis of the initial hard scattered parton will not be associated with the jet.

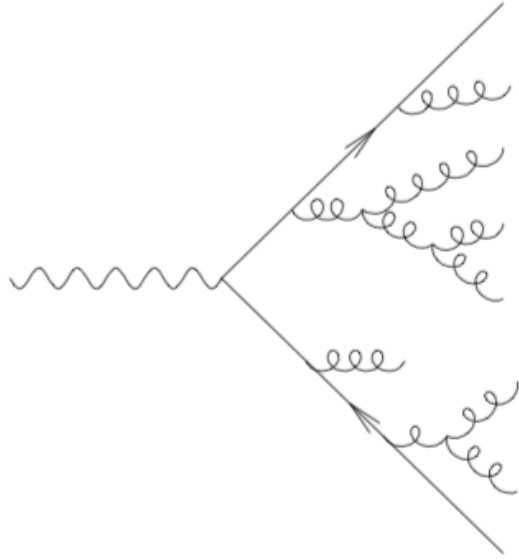


Figure 2.5: Parton cascade in a hadronic collision[18].

After the cascade has ended the partons must fragment into color neutral hadrons. There are two main phenomenological models used to describe the hadron forming process, the Lund String Model and the Cluster Hadronization Model. The QCD potential is,

$$V(r) = -\frac{\alpha_s}{r} + \sigma r \quad (2.8)$$

where the first term of Equation 2.8 goes as the Coulomb potential with a $1/r$ dependence and is the dominate term at short distance and the second term has a string-like potential with σ referring to a string-like tension. The Lund String Model ignores gluon radiation and has fragmentation occur via breaking the string tension with the production of $q\bar{q}$ sea quarks. The created sea quarks will carry some momentum fraction, z , of the initial parton until z falls below some cutoff. Figure 2.6 shows a two quarks undergoing a string breaking, each of the quarks initiating the string breaking will combine with a sea quark in an iterative manner to form hadrons.

The Cluster Hadronization Model has gluons splitting after the parton cascade phase into $q\bar{q}$ pairs. These pairs will form color-singlet clusters with other neighboring quarks in phase-space. These color-singlets will typically be a few GeV/c^2 in mass and are treated as

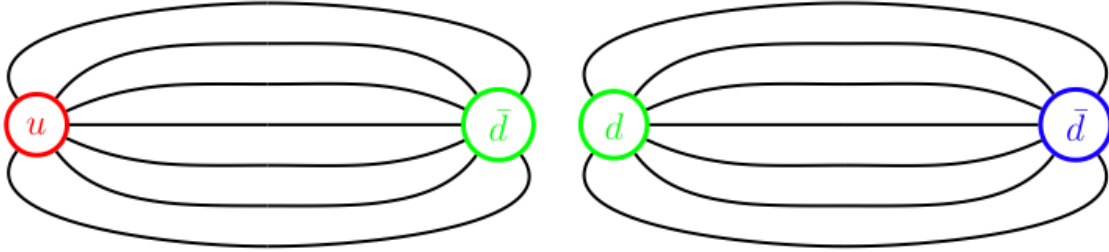


Figure 2.6: $u\bar{d}$ generating a $d\bar{d}$ pair via string breaking which will form color neutral hadrons, black lines show the string like equipotentials.[19].

excited meson resonances. These pseudo-resonances will decay via their normal branching ratios into the stable hadrons[20].

Fragmentation

The FF is similar to the PDF in that it is also a probability distribution. Ideally, the FF would be defined as the fractional momentum of the hadrons created from the fragmenting parton, $z \equiv p_{hadron}/p_{parton}$. Due to the confinement of partons we must use a suitable substitution for measuring the FF. The Parton-Hadron Duality[?] states that a hadron found near the center of a jet should encompass the quantum numbers and kinematic properties associated with the hard scattered quark that initiated the jet. Thus we can measure the fragmentation function as $z = p_{hadron}/p_{jet}$.

2.2.2 PYTHIA

PYTHIA[21], is a Monte Carlo software tool-kit used to model proton-proton collisions. The package uses pre-defined parton distribution functions as input and from their simulates partonic showers and radiation due to a hard scattering by generating the LO scattering matrix elements. Hadronization is performed in PYTHIA using the Lund String Model. After which relative branching ratios are used to statistically throw the decay modes of the hadrons.

2.2.3 PHOJET

2.2.4 HERWIG

2.2.5 FastJet

Although, it may simple to have a conceptual grasp of what a jet ‘is’ there is no unambiguous definition, both experimentally and theoretically, for how to define a jet. This is due to the fragmentation process by which partons form into their final state hadrons is not calculable pertubatively. The earliest jet measurements used multiple definitions which complicated comparisons between experiments and theoretical calculations. In 1990, the Snowmass Accord[22] was held in order to standardized the definition of a jet between experimentalists and theoreticians. The agreement maintained that any algorithm that clusters particles into a jet must be both infrared and collinear safe (IRC). If a high-momentum parton radiates a soft gluon this emission should not affect the

Although there are a number of jet finding algorithms available, I will only focus on algorithms that are both collinear and infrared safe.

2.3 Kinematics

Before I give a detailed discussion of the physics and observables in high energy and nuclear physics it would be advantageous to define some terms and go over a few formulas.

In a circular particle accelerator a beam of relativistic particles travels along a beamline. The coordinates along this beamline are broken into longitudinal and transverse component. The momentum can similarly be described in these coordinates as the longitudinal and transverse momentum, denoted as \mathbf{p}_L and \mathbf{p}_T . For cylindrical detectors like ALICE² it is more advantageous to use a cylindrical coordinate system of with θ as the polar angle and ϕ as the azimuth angle. Relativistic particles traveling along the beamline will have

$$y = \frac{1}{2} \ln \frac{E + |\mathbf{p}|}{E - |\mathbf{p}|} \quad (2.9)$$

²See Chapter ??

$$\eta = \frac{1}{2} \ln \frac{|\mathbf{p}| + p_L}{|\mathbf{p}| - p_L} \quad (2.10)$$

Therefore in terms of cartesian coordinates with the x-y plane as the plane transverse to the beamline and the z component as the component along the beam line we can derive the following relationships

$$p_x = p_T \cos \phi \quad (2.11)$$

$$p_y = p_T \sin \phi \quad (2.12)$$

$$p_z = p_T \sinh \eta \quad (2.13)$$

The advantage of using the azimuthal angle and psuedorapidity over cylindrical or Cartesian coordinates is that given any two particles, the separation between $R = \sqrt{(\phi_i - \phi_j)^2 + (\eta_i - \eta_j)^2}$ is invariant under all Lorentz boosts along the beamline.

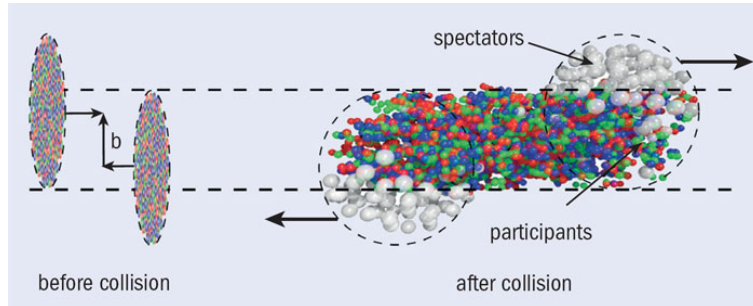


Figure 2.7: Nuclear collision .

In nuclear collisions the offset between the centers of two nuclei is known as the impact parameter (b) as seen in Figure 2.7. Measuring the impact parameter in an experimental setting is non-trivial and model-dependent. The distribution of nucleons in the nucleus is modeled after a Glauber distribution[23]. The Glauber model predicts that there is a direct correlation between the impact parameter of a nuclear collision and to the inelastic differential cross section (σ_{inel})[24].

$$c(b) = \frac{\int_0^b \frac{d\sigma}{db} db}{\int_0^\infty \frac{d\sigma}{db} db} = \frac{1}{\sigma_{inel}} \int_0^b \frac{d\sigma}{db} db \quad (2.14)$$

2.4 The Quark-Gluon Plasma

2.4.1 Asymptotic Freedom and the Perfect Fluid

Hydrodynamics

The conservation laws for a relativistic fluid conserve the charge current and energy-momentum tensor of the expanding fluid such that:

$$\partial_\mu N_i^\mu = 0 \quad (2.15)$$

$$\partial_\mu T^{\mu\nu} = 0 \quad (2.16)$$

2.4.2 Energy Loss in a Colored Medium

2.4.3 The Nuclear Modification Factor

2.4.4 Nuclear Collisions

2.5 QGP in Proton-Proton Collisions?

As previously stated a QGP is believed to be absent in proton-proton collisions, thus any signature of a QGP should likewise be absent. One way of quantifying the presence of the QGP is via the Bjorken energy density.

$$\varepsilon = \frac{1}{\tau A} \frac{dE_T}{d\eta} \quad (2.17)$$

where A is the transverse area of the nuclei, τ is the proper time, and $dE_T/d\eta$ is the transverse energy per unit pseudorapidity. It can be shown that the 150 MeV critical temperature need for the phase transition to the QGP corresponds to $1 - 3 \text{GeV}/fm^3$ energy density. The quantity $dE_T/d\eta$ can be related to the mean transverse momentum $\langle p_T \rangle$ and particle multiplicity³ per unity pseudorapidity as:

³Multiplicity is defined as the number of particles per event

$$\frac{dE_t}{d\eta} \approx \langle p_T \rangle \frac{dN}{d\eta} \quad (2.18)$$

where $\langle p_T \rangle$ is the mean transverse momentum and $dN/d\eta$ is the particle multiplicity per unit pseudorapidity. This suggest that in very high multiplicity proton-proton events signatures of the QGP may be present. This is one of the most active and newest areas of research in heavy ion physics.

Chapter 3

The ALICE TPC Upgrade

From 2014 until 2018, I worked on the upgrade of the TPC to a continuous readout. This includes working on a test beam in 2014 for a prototype Read-Out Chamber (ROCs) using Micropattern Gaseous Detectors (MPGD) over the current Multi-Wire Proportional Chamber (MWPC) design. Once a final design for the new ROCs was chosen the production of the new Inner Read-Out Chambers (IROCs) using a stack of four Gaseous Electron Multiplier (GEM) foils took place at the University of Tennessee. During this period I assembled 49 new IROCs. In 2018, I traveled to Yale University and CERN to help with quality assurance of the IROCs built at Tennessee.

3.0.1 Physics Motivation

After the 2018 heavy-ion run ends, the LHC will begin the second long shutdown (LS2) and upgrade to the High Luminosity LHC (Hi-Lumi LHC)[25] which was briefly mentioned in section ???. The goal of the LHC upgrade is to move into an era of high precision measurements of rare QCD processes and increase the production of soft probes. Once the upgrade is complete the expected event rate in ALICE will be 50 kHz in MinBias PbPb collisions. This will lead to a factor of x100 increase in MinBias data and a factor of x10 increase in high- p_T triggered data recorded by ALICE.

The ALICE experiment has focused on probing the thermodynamic properties of the QGP in the past. The increase in event rate expected from the Hi-Lumi LHC would open new ways to probe the QGP including[26]:

- Increasing the production of jets and allowing separation of jet measurements based on the flavor of the initial parton.
- Studying the production mechanisms of light-nuclei, antihyper-nuclei, and other exotic hadrons.
- Probing the initial state temperature and equation of state of the QGP by measuring low-mass dileptons that originate from the earliest stages of a heavy-ion collision.
- Increase the yields of heavy-flavor mesons reconstructed via the secondary-vertices.

In order to do this ALICE will implement a number of upgrades [27] during the shutdown that include:

- Replacing the V0 and T0 detectors with a combined detector, called the Forward Interaction Trigger (FIT)[28].
- Improving the ITS and Muon Tracker spatial resolution by using Monolithic Active Pixel Sensors (MAPS)[29][30].
- Removing the 400 nanosecond dead time associated with the TPC and upgrade the FEE cards to handle the increase in data bandwidth[26].
- New Online/Offline (O^2) data processing architecture[31].

Leptons weakly couple to the QGP[32] and by studying these the initial states in heavy ion collisions may be probed[33]. Figure 3.1 shows a simulation of the mass spectra for dileptons between $0 \text{ GeV}/c - 1 \text{ GeV}/c$ using the current ALICE central detectors with tight kinematic cuts (left). The yields that are quantifiable do not allow for the separation of leptons originating from the QGP from those originating from background sources. After the increase in event rate and the upgraded ITS with improved tracking capabilities, measuring

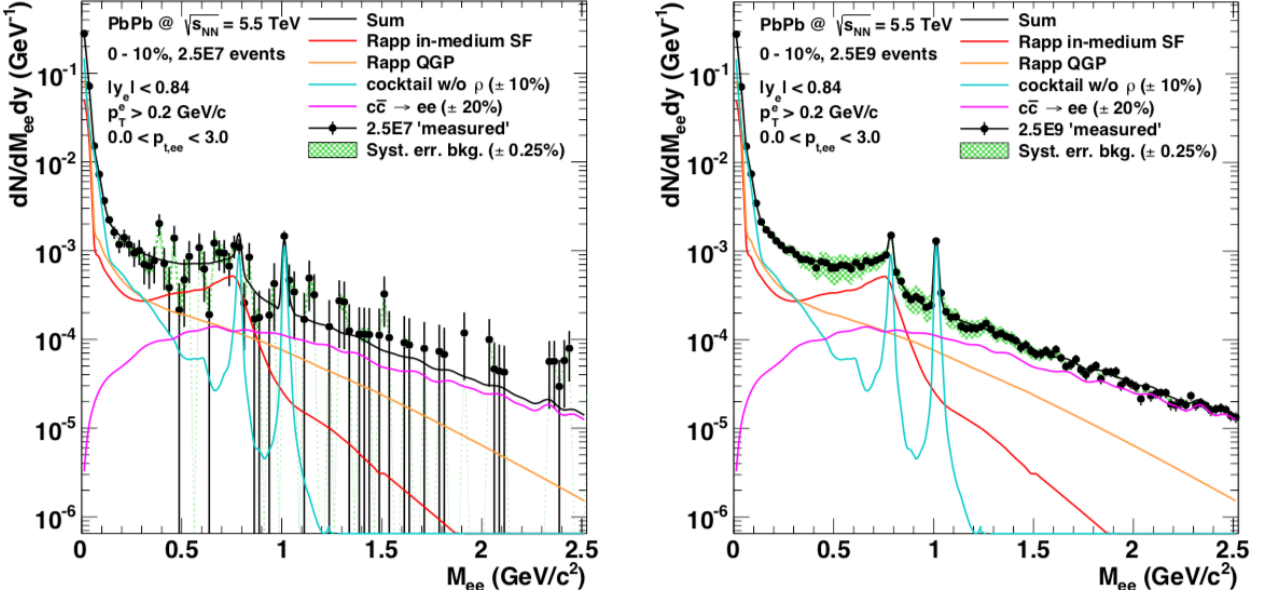


Figure 3.1: Simulation of the invariant mass spectra for dileptons in a typical heavy-ion run with current ALICE performance (left) and after upgrade of ALICE for Run-3 (right) in PbPb at $\sqrt{s_{NN}} = 5.5$ TeV. The dilepton yields originating from the QGP are shown (red and orange), along with background contributions from light-hadrons (blue), and charm (magenta)[26].

the low-mass dileptons that interacted with the QGP will be possible as shown on the right of Figure 3.1.

The TPC used in the ALICE experiment along with the readout was discussed in section ???. The ALICE collaboration first proposed an upgrade of the TPC in 2012 with a Letter of Intent (LoI)[26]. A Technical Design Report(TDR)[34] was published in 2013 with an initial design overview. An addendum to the TDR[35] was published in 2015 after the performance of prototype ROCs was measured on a test beam at CERN in 2014. The overall goals of the TPC upgrade are to continuously readout events in the high luminosity environment expected after LS2, to minimize the accumulation of space-charge distortions in the drift field, and to maintain the PID and tracking performance of the current TPC.

3.0.2 Gaseous Electron Multiplier Foils

Gaseous Electron Multiplier (GEM) Foils were first proposed by CERN physicist Fabio Sauli in 1997[36]. GEMs belong to a new form of detector technology known as Micropattern

Gaseous Detectors[37] that use microelectronic or chemical etching techniques to print a readout structure onto a material surface.

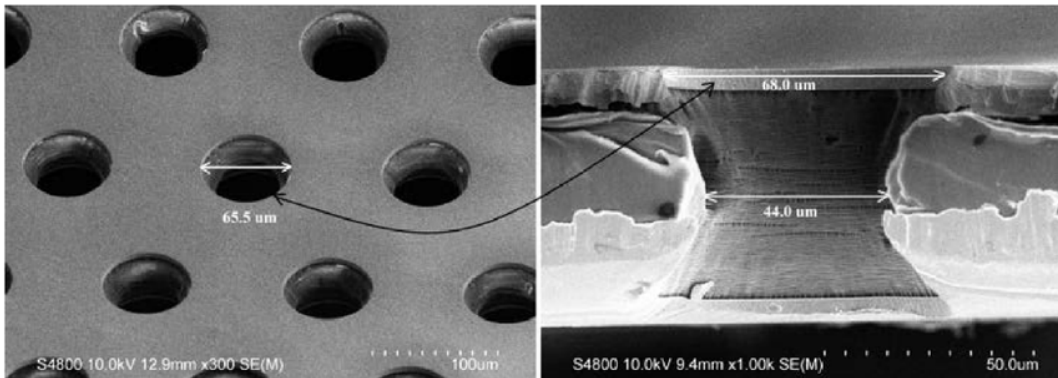


Figure 3.2: Scanning electron microscope image of a GEM foil from top (left) and profile (right)[38].

GEM foils are a Kapton sheet, typically $50 \mu m$ thick, with a thin copper coat on both sides of the surface. A weak acid and stencil are used to chemically etch holes throughout the foil. Typically, the holes are between $10 \mu m$ - $100 \mu m$ in diameter and between $100 \mu m$ - $300 \mu m$ in pitch as seen in Figure 3.2. A few hundred volts is applied to each of the copper surfaces of the GEM foil causing a strong electric field to be induced in the GEM holes¹.

When a ionization electron from a charged track enters a GEM hole it will cause an avalanche of electrons and ions to be produced, amplifying the signal, to MWPCs. Due to the high voltage and strong electric fields around the GEM foil, any back flow ions created from the avalanche will get absorbed by the copper surfaces on the GEM foil, as seen in Figure 3.3.

The configuration of the pitch and size holes on a GEM foil is directly correlated to the amplification properties and ability to capture back flow ions. GEMS with larger holes or shorter pitch between the holes will have more amplification but will also be more ineffective at capturing ions. Likewise, GEMs with shorter holes or larger pitch will have better ion capture abilities yet worse amplification properties. By stacking multiple GEMs on top of one another it is possible to maximize the amplification properties and minimize the backflow.

Creating GEMs with a uniform hole distribution and stacking them in a consistent manner in order to minimize the overlap of holes from one layer to another restricted

¹The electric field is on the order of 10 kV/cm

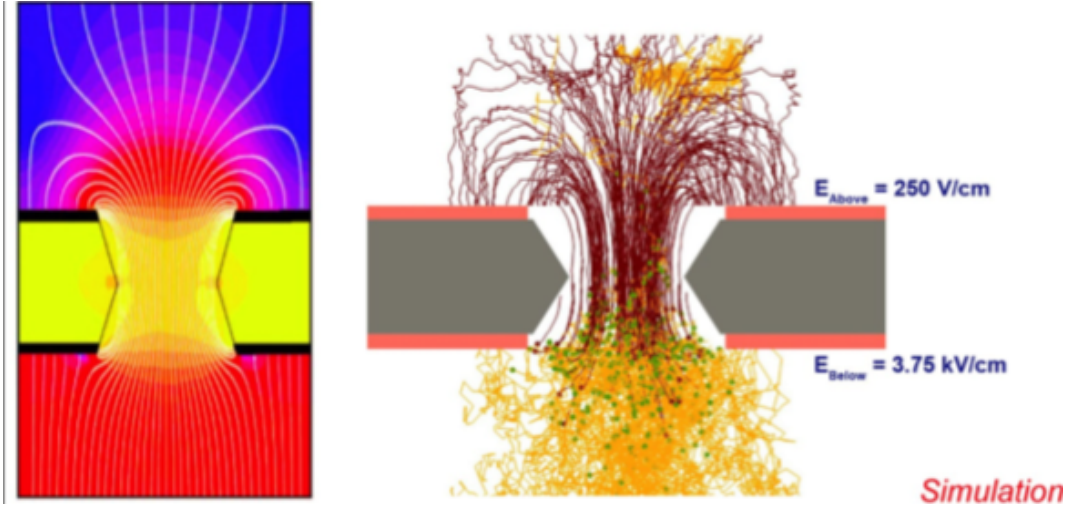


Figure 3.3: Profile of GEM with electric-field lines and gradients (left). Simulation of an ionization electron (yellow line) entering a GEM from a drift volume, amplification electrons (green dots, yellow lines) and back flow ions (red lines) are created (right)[39].

them to small prototypes and impeded their use on large experiments. Around 2010 two methods were developed, the single-mask technique[40] and the NS2 assembly[41], which allowed for a systematic way of etching holes and stretching GEMs so they could be properly aligned. These methods allowed for GEMs to become a viable amplification device for large experiments. As of 2018 the TOTEM, COMPASS, ATLAS, and LHCb experiments have all incorporated GEMs in their trackers. Future colliders, such as the Electron-Ion Collider (EIC), plan on using them[42].

3.0.3 Research and Development

Initially, it was decided that the new ROCs would incorporate a stack of three GEMs with a hole geometry similar to the one incorporated on the LHCb experiments[43] tracking detector. This was a starting point to bench mark performance for the ALICE TPC upgrade as well as an opportunity to use experts in GEM technology already present at CERN. The first phase of the R&D involved simulating the performance of the LHCb 3-GEM stack in the high event rate environment expected after the Hi-Lumi LHC upgrade using a the software package called Garfield++[?], which is a GEANT4[44] add-on package built to simulate MPGDs. It was quickly observed from the simulations that a 3-GEM stack would

be insufficient in maintaining the performance needed for the TPC while minimizing the ion back flow. An additional layer of GEM was added to the 3-GEM stack in simulation and it was observed that this configuration would preserve the TPC performance.

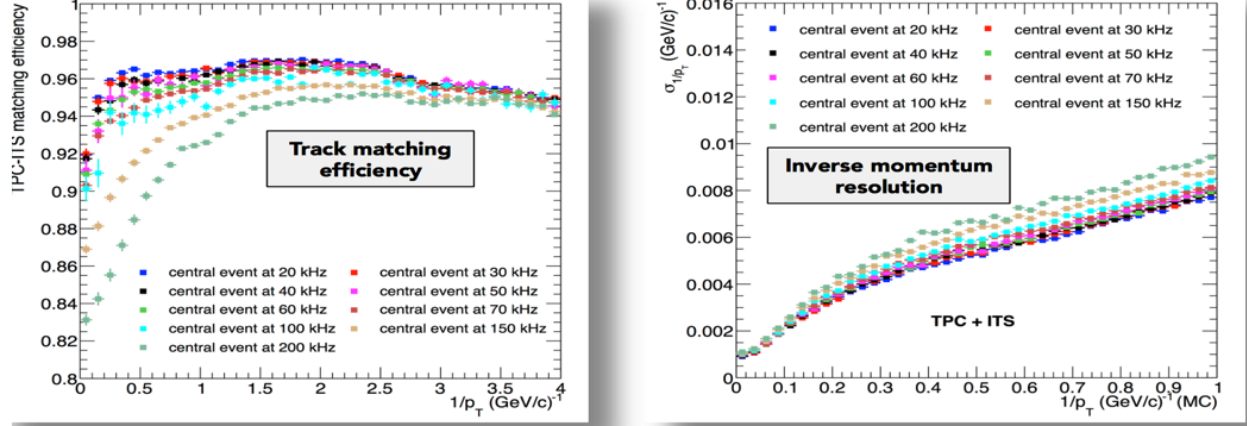


Figure 3.4: ITS-TPC matching (*left*) and inverse momentum resolution (*right*) for a 4-GEM stack simulated in Garfield++ [45].

Figure 3.4 shows simulations of the track matching efficiency from the ITS to the TPC and the inverse momentum resolution for a 4-GEM stack as a function of several collisions. The efficiency and resolution only start to diminish at an event rate above 100 kHz, which is double the expected rate after the LHC upgrade, and are well within the range of the current TPC operating at 3.5 kHz.

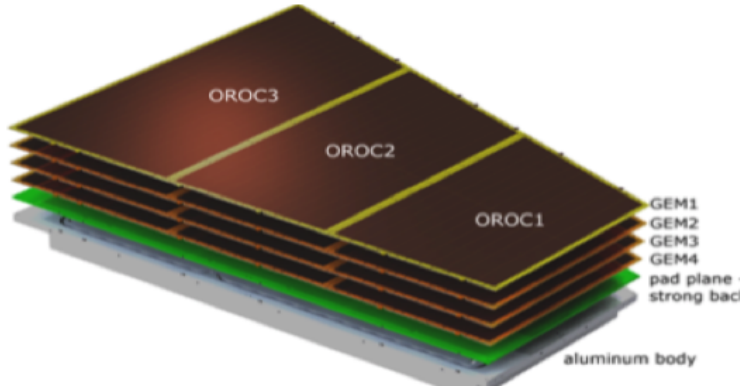


Figure 3.5: Final design of the upgraded readout chambers with a stack of 4 GEMS [34].

The optimal hole configuration was also explored with simulations. Having a first and forth layer with a pitch of $140 \mu m$ and the second and third layer with a pitch of $280 \mu m$, allowed for the the ROCs to maintain minimal ion backflow while amplifying the signal from

tracks. Figure 3.5 shows the design of the ROCs with a 4-GEM stack. The copper pad plane is glued to a reinforced fiberglass sheet, known as the strongback, to add material strength.

2014 Test Beam

During the 2014 test beam, I mounted the prototypes on the beam line, recorded data from the test beam, and monitored the performance in real time. To quantify the performances of the prototype, it is useful to define the effective gain (G_{eff}) and ionic backflow (IBF%)

$$G_{eff} = \frac{I_{anode}}{e N_{ion} R} \quad (3.1)$$

where e is the fundamental electric charge of an electron, N_{ion} is the number of captured ions, and R is the illumination rate from an active source.

$$IBF\% = \frac{I_{cathode}}{I_{anode}} = \frac{1 + \epsilon}{G_{eff}} \quad (3.2)$$

where $I_{cathode}/I_{anode}$ is the ratio of the currents measured in the cathode and anode portion of a readout as seen in Figure ???. The IBF% can also be defined in terms of the number of backflowing ions (ϵ) created at an effective gain (G_{eff}). The effective gain is a measure of the amplification properties and in a gaseous detector is defined as

The test involved using the beam from both the SPS and PS² at the LHC cast onto an iron target. This iron target created secondary showers and tracks were measured by the prototype for both energy resolution and PID performance. The nominal TPC gas of $CO_2 - N_2$ (90-10) was used during the test beam.

Figure 3.6 shows the PID performance for separating electron and pion tracks created by the iron target. The separation power between the two Gaussian peaks increases until a gain of 2000 so this was chosen as the target effective gain for the new ROCs.

Figure 3.7 shows the energy resolution of the iron peak as a function of the relative voltages between GEM 2 (U_{GEM2}) and the ratio of voltages between GEM 3 (U_{GEM3}) and GEM 4 (U_{GEM4}). This shows that the IBF% remains below 1% at a energy resolution of approximately 10% which is consistent with the current TPC performance. The voltages

²See Section ??.

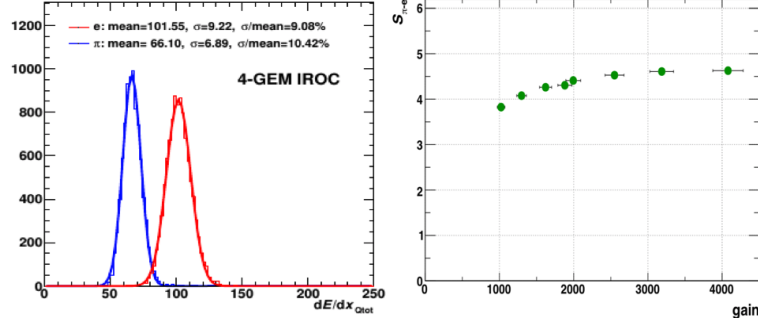


Figure 3.6: dE/dx resolution of the 4-GEM IROC prototype (*left*) and the separation power between electrons and pions as a function of gain (*right*) [35].

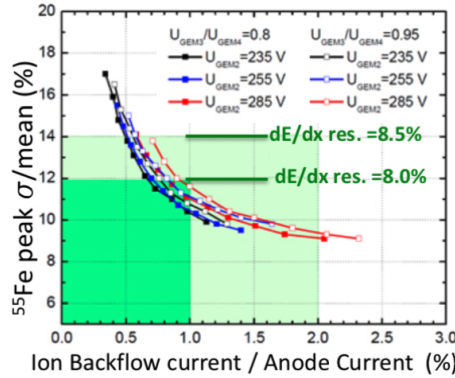


Figure 3.7: Energy resolution of the iron peak as measured from the prototype IROC with varying GEM voltages as a function of IBF% [35].

were chosen such that GEM 1 and GEM2, which are closest to the drift volume, would focus mostly on capturing amplification ions while GEM 3 and GEM 4, which are closest to the copper pad readout, would primarily perform the amplification as shown in Figure 3.8.

3.0.4 Production of the Inner Readout Chambers in the U.S.

Once a final design was settled on from the simulation and prototype R&D, the project entered the production phase. A minimum of 36 new ROCs would need to be built with the 4-GEM stack to replace the old ROCs in the TPC while 4 additional ROCs would be constructed as spares. Due to the size and weight of the ROCs, production of the IROCs would take place in the United States and the OROC production mainly in Germany.

Figure 3.13 shows the production flow for the construction of the 4-GEM ROCs. After GEMs are received from the manufacturer, they go through a number of quality assurance tests

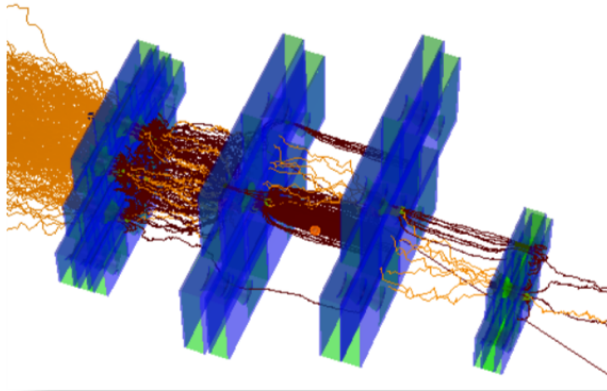


Figure 3.8: Simulation of the four GEM (blue) layers after test beam. The configuration is such that the two GEMs closest to the drift volume, right side, absorb the amplification ions created by the two GEMs closest to the readout (right) [35].

before they are shipped to Wayne State University, where they are stretched and mounted for the IROCs. The aluminum bodies are manufactured at the University of Texas Austin and shipped to Tennessee. At Tennessee we glue the pad plane, aluminum body and strong back together before it is shipped to Yale, where the chambers are fit with the GEMs from Wayne State. The production steps for the OROC mirror those performed by the IROC except that it was performed mainly German institutes.

Figure 3.10 shows the procedure followed at Tennessee in order to build an IROC. Furthest on the left is a picture of a copper pipe glued into the aluminum body. This copper pipe is flushed with a coolant that maintains the temperature of the Front End Electronics (FEE). The next two photos show the pad plane being mounted on a vacuum table while glue is applied to it and the aluminum body. Once all the components are placed glued and mounted on the table the IROC is loaded with lead bricks and allowed to cure for 24 hours. The right most picture shows the final step of the HV feedthroughs mounted and glued for the GEM foils. Before a completed IROC leaves Tennessee we performed a gas tightness test that will be discussed more in the next section. Full production of the IROCs ended in November of 2018 with a total of 47 chambers being built at Tennessee. A surplus of chambers were built with excess materials to provide spares.

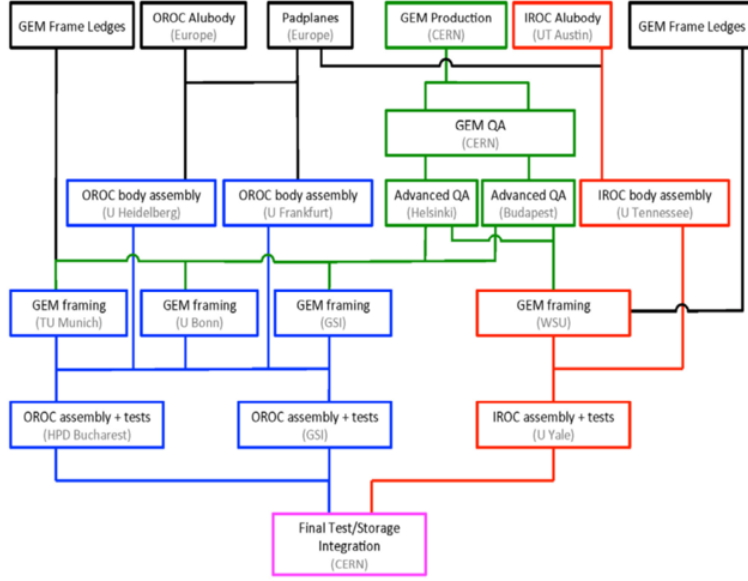


Figure 3.9: Production flow of the IROCs (red), OROCs (blue), and GEM foils (green)[45].



Figure 3.10: The author assembling an Inner Readout Chamber at the University of Tennessee.

3.0.5 GEM and Chamber Quality Assurance

A stringent set of quality assurance (QA)[46][38] protocols were implemented to monitor any damage sustained during transport and to quickly identify any flaws in the production procedures. The QA can be broken into two major categories: QA performed on the GEM foils as received from the manufacturer and QA performed on complete/semi-complete

chambers as they were going through the different production steps. I will discuss only the QA tasks that I was directly involved with.

GEM QA

In order to evaluate the performance of a GEM foil, a spark test was performed on every foil. Sparks are caused by the discharge of the foil and may be due to the presence of dust on a foil, imperfections in the hole geometry, or a short between the two copper layers of the GEM. The final design of the GEM foils had each foil segmented into twelve sectors with a $10 M\Omega$ bias resistor across every segment. Any sparks that occur on the GEM will only discharge a given segment and not the entire foil. Because of the delicate nature of the GEM foil, sparks have the potential to permanently damage a foil or seriously affect the performance of a ROC. Thus GEMs with a high spark rate should be excluded as soon as possible in the production flow.

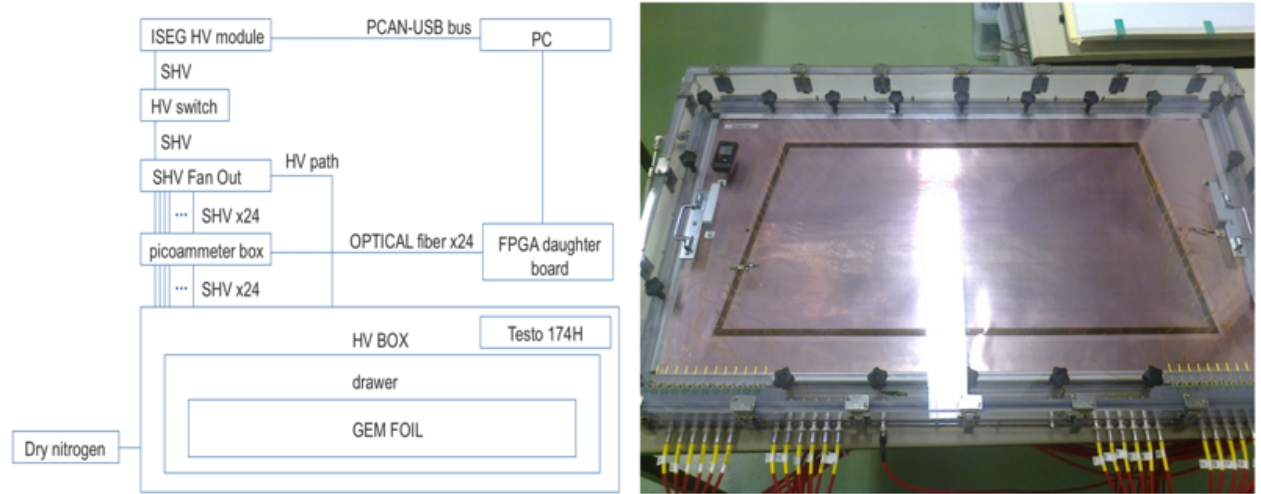


Figure 3.11: Schematic for the setup of the GEM foil spark test (*left*)^[46] and the GEM mounted in the HV gas box (*right*).

The GEM foil spark test involves mounting each foil in a High Voltage (HV) box, which is flushed with N_2 until it reaches a relative humidity of $\approx 10\%$. Once this humidity is reached 500 V is placed across each segment of the GEM and monitored with a LabView interface. A spark is defined as the LabView recording a current above 10 nA across the bias resistor through any GEM segment and read by a multi-channel picoammeter. The criteria for a GEM to fail this QA was to have more than five sparks over a 20 minute recording window.

Chamber QA

Most of the QA I helped with was on ROC chambers as they went through the production steps. Before completed IROC chambers were sent to Yale, I performed a gas leak test. The leak test consisted of mounting an individual chamber into an aluminum test vessel and flushing the inside of the vessel with N_2 gas. By using a flowmeter to measure the rate that N_2 gas enters the test vessel and an oxygen sensor to measure the amount of oxygen present at the output of the test vessel we can infer the leak rate of each IROC chamber. Figure 3.12 shows a schematic of the setup (left) and what the typical output from the LabView interface (right). By flowing at two different rates and measuring the oxygen content at each rate we could confirm the leak rate.

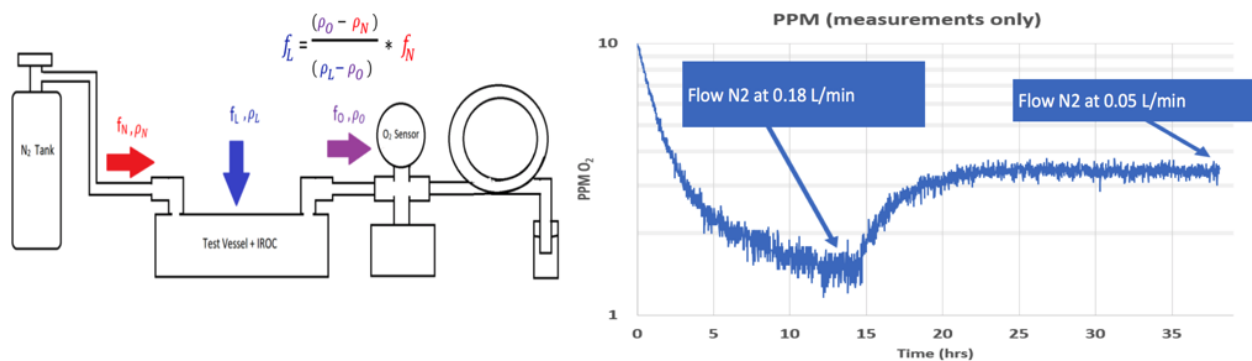


Figure 3.12: Schematic of the gas tightness testing setup at the University of Tennessee (*Courtesy of Joseph Rasson*).

The leak rate of a chamber, f_L , can be quantified as

$$f_L = \left(\frac{\rho_0 - \rho_N}{\rho_L - \rho_0} \right) f_N \quad (3.3)$$

where f_N is the flow rate of N_2 gas into the test vessel, ρ_L is the concentration of O_2 in the laboratory, ρ_N is the O_2 impurity present in the N_2 bottle, and ρ_0 is the O_2 reading from the LabView interface.

A maximum leak rate of 0.25 mL/hour was placed as the rejection criteria for a given chamber. If a chamber had a leak rate above this the N_2 gas could get swapped out with a helium gas tank and we could use a helium sniffer to identify the areas on the IROC

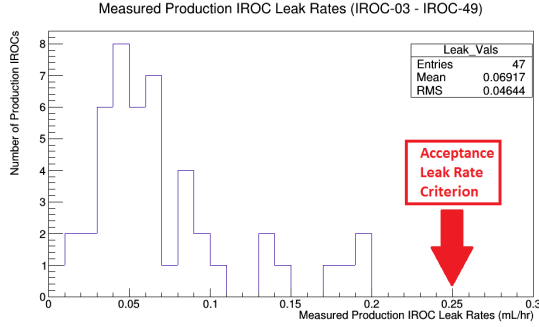


Figure 3.13: Leak rate of the 47 chambers built at Tennessee with the maximum failure rate at 0.25 ml/hr shown (*Courtesy of Charles Hughes*).

causing the leak and patch the area with epoxy. Figure 3.13 shows the leak rate for all IROCs produced at Tennessee, due to none of the chambers surpassing the leak threshold the helium sniffer was not used in the production of the IROCs.

Once an IROC chamber was fitted with the 4 GEM foils at Yale and sent to CERN a spark test was performed over the entire chamber. The test involved placing each chamber next to the LHC beam line, flushing with the nominal TPC gas, and placing the nominal voltage across each GEM and monitoring the spark rate once a beam was present in the LHC. Figure 3.14 shows myself installing the completed IROC chambers next to the LHC beam line in front of ALICE and the output from the spark monitor. The voltage across each chamber could be varied in real time in order to minimize sparking while maintaining the IROC performance, thus reducing the rate of degradation on a per chamber basis once installed in the TPC.

3.0.6 Outlook

As of November 2018, the 47 IROCs assembled at Tennessee have been received at CERN. None of the built chambers have surpassed the gas leak test performed at CERN and so far only 4 chambers exhibit sparking rates above the threshold. By May of 2019, the LHC beamline around ALICE will be decommissioned and the TPC will be moved to a surface level clean room for the installation of the chambers. The installation of the new FEE electronics and the ROC chambers should take place throughout the summer of 2019. Afterwards there will be a 10 month commissioning with the TPC, during which the performance of the

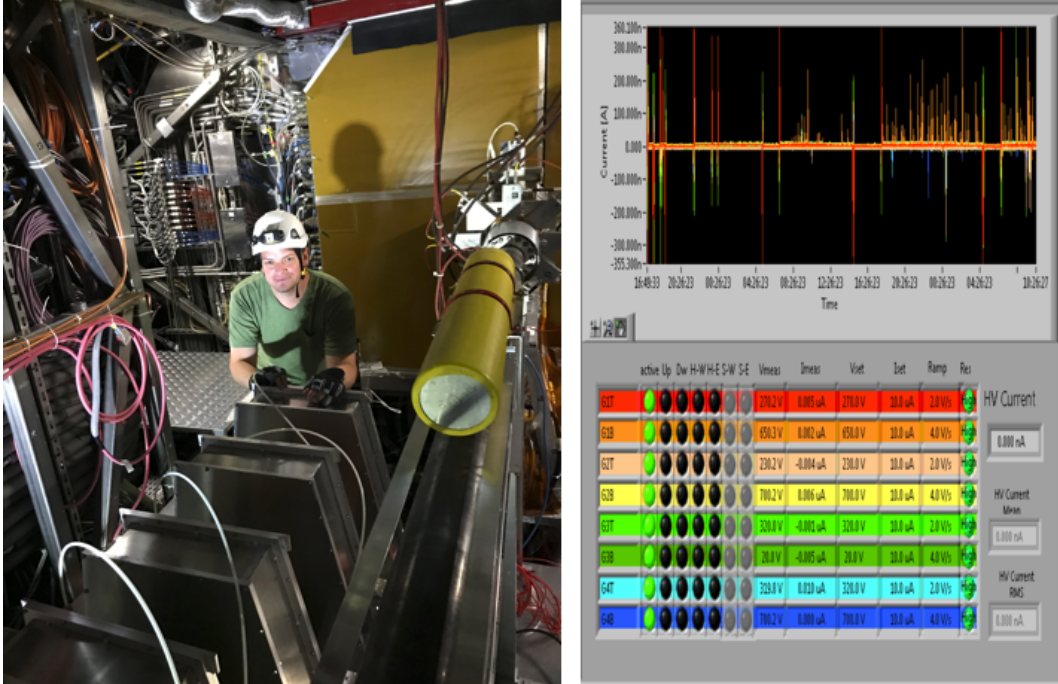


Figure 3.14: The author testing spark testing chambers next to the LHC beam line (*left*) and real time output from the spark test during a live beam (*right*).

upgraded TPC will be evaluated with cosmic rays. By the end of 2020, the TPC should be back in the ALICE cavern and the beam line will have been re-installed. The Hi-Lumi run of the LHC is expected to start in March of 2021.

Bibliography

- [1] C. Patrignani et al. Review of Particle Physics. *Chin. Phys.*, C40(10):100001, 2016. [1](#), [38](#)
- [2] Paul Langacker. Introduction to the Standard Model and Electroweak Physics. In *Proceedings of Theoretical Advanced Study Institute in Elementary Particle Physics on The dawn of the LHC era (TASI 2008): Boulder, USA, June 2-27, 2008*, pages 3–48, 2010. [1](#)
- [3] Tatsumi Aoyama, M. Hayakawa, Toichiro Kinoshita, and Makiko Nio. Tenth-Order Electron Anomalous Magnetic Moment — Contribution of Diagrams without Closed Lepton Loops. *Phys. Rev.*, D91(3):033006, 2015. [Erratum: *Phys. Rev.*D96,no.1,019901(2017)]. [2](#)
- [4] Michael Riordan. The discovery of quarks. *Science*, 256(5061):1287–1293, 1992. [4](#)
- [5] Frank Wilczek. Asymptotic freedom: From paradox to paradigm. *Proc. Nat. Acad. Sci.*, 102:8403–8413, 2005. [Rev. Mod. Phys.77,857(2005)]. [5](#)
- [6] Vardan Khachatryan et al. Measurement of the inclusive 3-jet production differential cross section in proton–proton collisions at 7 TeV and determination of the strong coupling constant in the TeV range. *Eur. Phys. J.*, C75(5):186, 2015. [5](#)
- [7] J. D. Bjorken. Asymptotic sum rules at infinite momentum. *Phys. Rev.*, 179:1547–1553, Mar 1969. [6](#)
- [8] J. D. Bjorken. Can We Measure Parton Parton Cross-Sections? *Phys. Rev.*, D8:4098, 1973. [6](#)
- [9] Matt Dobbs and Jorgen Beck Hansen. The HepMC C++ Monte Carlo event record for High Energy Physics. *Comput. Phys. Commun.*, 134:41–46, 2001. [7](#)
- [10] Wolfgang Kurt Hermann Panofsky. Low q electrodynamics, elastic and inelastic electron (and muon) scattering. 1968. [8](#)
- [11] J. Feltesse. Introduction to Parton Distribution Functions. *Scholarpedia*, 5(11):10160, 2010. revision #186761. [9](#)

- [12] K. Kovarik, T. Jezo, A. Kusina, F. I. Olness, I. Schienbein, T. Stavreva, and J. Y. Yu. CTEQ nuclear parton distribution functions. *PoS*, DIS2013:274, 2013. [8](#)
- [13] Richard D. Ball, Valerio Bertone, Stefano Carrazza, Christopher S. Deans, Luigi Del Debbio, Stefano Forte, Alberto Guffanti, Nathan P. Hartland, José I. Latorre, Juan Rojo, and Maria Ubiali. Parton distributions for the LHC Run II. *JHEP*, 04(arXiv:1410.8849. EDINBURGH 2014-15. IFUM-1034-FT. CERN-PH-TH-2013-253. OUTP-14-11P. CAVENDISH-HEP-14-11):040. 138 p, Oct 2014. Comments: 138 pages, 64 figures. Several typos in text and references corrected, one reference added. [8](#)
- [14] Harald Fritzsch. QCD: 20 years later. In *QCD 20 Years Later: Proceedings, Workshop, Aachen, Germany, June 9-13, 1992*, pages 827–852, 1992. [9](#), [10](#)
- [15] John C. Collins, Davison E. Soper, and George F. Sterman. Factorization of Hard Processes in QCD. *Adv. Ser. Direct. High Energy Phys.*, 5:1–91, 1989. [9](#)
- [16] Nora Brambilla, Xavier Garcia i Tormo, Joan Soto, and Antonio Vairo. The Logarithmic contribution to the QCD static energy at $N^{**}4$ LO. *Phys. Lett.*, B647:185–193, 2007. [10](#)
- [17] Martin Erdmann. Investigation of quark - anti-quark interaction properties using leading particle measurements in e+ e- annihilation. *Phys. Lett.*, B510:29–35, 2001. [10](#)
- [18] B. R. Webber. Hadronization. In *Proceedings: Summer School on Hadronic Aspects of Collider Physics, Zuoz, Switzerland, Aug 23-31, 1994*, pages 49–77, 1994. [10](#), [11](#)
- [19] Bo Andersson, Sandipan Mohanty, and Fredrik Soderberg. Recent developments in the Lund model. In *36th Annual Winter School on Nuclear and Particle Physics (PINP 2002) and 8th St. Petersburg School on Theoretical Physics St. Petersburg, Russia, February 25-March 3, 2002*, 2002. [12](#)
- [20] B. R. Webber. A QCD Model for Jet Fragmentation Including Soft Gluon Interference. *Nucl. Phys.*, B238:492–528, 1984. [12](#)

- [21] Torbjorn Sjostrand, Stephen Mrenna, and Peter Z. Skands. A Brief Introduction to PYTHIA 8.1. *Comput. Phys. Commun.*, 178:852–867, 2008. [12](#)
- [22] J E Huth, N Wainer, K Meier, N J Hadley, F Aversa, Mario Greco, P Chiappetta, J P Guillet, S Ellis, Zoltán Kunszt, and Davison Eugene Soper. Toward a standardization of jet definitions. (FERMILAB-CONF-90-249-E):7 p, Dec 1990. [13](#)
- [23] Constantin Loizides. Glauber modeling of high-energy nuclear collisions at the subnucleon level. *Phys. Rev.*, C94(2):024914, 2016. [14](#)
- [24] Michael L. Miller, Klaus Reygers, Stephen J. Sanders, and Peter Steinberg. Glauber modeling in high energy nuclear collisions. *Ann. Rev. Nucl. Part. Sci.*, 57:205–243, 2007. [14](#)
- [25] G Apollinari, I Béjar Alonso, O Brüning, M Lamont, and L Rossi. High-Luminosity Large Hadron Collider (HL-LHC) : Preliminary Design Report. 2015. [17](#)
- [26] B Abelev et al. Upgrade of the ALICE Experiment: Letter of Intent. Technical Report CERN-LHCC-2012-012. LHCC-I-022. ALICE-UG-002, CERN, Geneva, Aug 2012. [18](#), [19](#)
- [27] Levente Molnar and the ALICE Collaboration. Upgrade and physics perspective of alice at the lhc. *Journal of Physics: Conference Series*, 589(1):012014, 2015. [18](#)
- [28] T L Karavicheva and ALICE Collaboration. The fast interaction trigger detector for the alice upgrade. *Journal of Physics: Conference Series*, 798(1):012186, 2017. [18](#)
- [29] B Abelev and all. Technical Design Report for the Upgrade of the ALICE Inner Tracking System. Technical Report CERN-LHCC-2013-024. ALICE-TDR-017, Nov 2013. [18](#)
- [30] Technical Design Report for the Muon Forward Tracker. Technical Report CERN-LHCC-2015-001. ALICE-TDR-018, Jan 2015. [18](#)
- [31] P Buncic, M Krzewicki, and P Vande Vyvre. Technical Design Report for the Upgrade of the Online-Offline Computing System. Technical Report CERN-LHCC-2015-006. ALICE-TDR-019, Apr 2015. [18](#)

- [32] Radoslaw Ryblewski and Michael Strickland. Dilepton production from the quark-gluon plasma using leading-order (3+1)D anisotropic hydrodynamics. *Acta Phys. Polon. Supp.*, 8(2):445, 2015. [18](#)
- [33] Mauricio Martinez and Michael Strickland. Measuring QGP thermalization time with dileptons. *Phys. Rev. Lett.*, 100:102301, 2008. [18](#)
- [34] Upgrade of the ALICE Time Projection Chamber. Technical Report CERN-LHCC-2013-020. ALICE-TDR-016, Oct 2013. [19](#), [22](#)
- [35] Addendum to the Technical Design Report for the Upgrade of the ALICE Time Projection Chamber. Technical Report CERN-LHCC-2015-002. ALICE-TDR-016-ADD-1, Feb 2015. [19](#), [24](#), [25](#)
- [36] F. Sauli. GEM: A new concept for electron amplification in gas detectors. *Nucl. Instrum. Meth.*, A386:531–534, 1997. [19](#)
- [37] Maxim Titov. Perspectives of Micro-Pattern Gaseous Detector Technologies for Future Physics Projects. In *Proceedings, CMS Workshop: Perspectives on Physics and on CMS at Very High Luminosity, HL-LHC: Alushta, Crimea, Ukraine, May 28–31, 2012*, pages 241–258, 2013. [20](#)
- [38] Erik Brücken and Timo Hildén. GEM Foil Quality Assurance For The ALICE TPC Upgrade. *EPJ Web Conf.*, 174:03004, 2018. [20](#), [26](#)
- [39] Purba Bhattacharya, Bedangadas Mohanty, Supratik Mukhopadhyay, Nayana Majumdar, and Hugo Natal da Luz. 3D simulation of electron and ion transmission of GEM-based detectors. *Nucl. Instrum. Meth.*, A870:64–72, 2017. [21](#)
- [40] M Tang, A Q Liu, A Agarwal, and M H Habib. A single-mask substrate transfer technique for the fabrication of high-aspect-ratio micromachined structures. *Journal of Micromechanics and Microengineering*, 17(8):1575, 2007. [21](#)
- [41] W. You, Y. Zhou, J. Liu, M. Shao, C. Li, H. Chen, Z. Tang, Y. Sun, Y. Zhang, Y. Lv, G. Song, X. Wang, D. Hu, and D. Hong. A new technique for assembling large-size gem detectors. *Journal of Instrumentation*, 12(06):C06036, 2017. [21](#)

- [42] Fabio Sauli. The gas electron multiplier (gem): Operating principles and applications. *Nuclear Instruments and Methods in Physics Research Section A: Accelerators, Spectrometers, Detectors and Associated Equipment*, 805:2 – 24, 2016. Special Issue in memory of Glenn F. Knoll. [21](#)
- [43] Marco Santimaria and Davide Pinci. Study of the GEM detector for the LHCb experiment upgrade, Nov 2013. Presented 19 Dec 2013. [21](#)
- [44] S. Agostinelli et al. GEANT4: A Simulation toolkit. *Nucl. Instrum. Meth.*, A506:250–303, 2003. [21](#)
- [45] Dick Majka. The alice tpc upgrade project. Quark Matter 2017, 2017. [22](#), [26](#)
- [46] Jens Erik Brückner and Timo Eero Hildén. The GEM QA Protocol of the ALICE TPC Upgrade Project. In *5th International Conference on Micro Pattern Gas Detectors (MPGD2017) Temple University, Philadelphia, USA, May 22-26, 2017*, 2018. [26](#), [27](#)
- [47] Francesco Noferini. The ALICE PID performance in Run 1 and perspectives in view of Run 2. In *Proceedings, 3rd Large Hadron Collider Physics Conference (LHCP 2015): St. Petersburg, Russia, August 31-September 5, 2015*, pages 523–528, Gatchina, 2016. Kurchatov Institute, Kurchatov Institute. [39](#)
- [48] Betty Bezverkhny Abelev et al. Production of charged pions, kaons and protons at large transverse momenta in pp and Pb–Pb collisions at $\sqrt{s_{\text{NN}}} = 2.76$ TeV. *Phys. Lett.*, B736:196–207, 2014. [39](#)

Appendices

A Particle Identification via Bethe-Bloch

The energy loss of a relativistic charged particle traversing through a medium is given by the Bethe-Bloch relation:

$$\frac{dE}{dx} \propto \frac{1}{\beta^2} \frac{Z}{A} \rho \left[\frac{1}{2} \ln \frac{2m_e c^2 \beta^2 \gamma^2 T_{max}}{I^2} - \beta^2 - \frac{\delta(\beta\gamma)}{2} \right] \quad (4)$$

where ρ is the density of the medium, $\frac{Z}{A}$ is the ratio of the atomic number to the atomic mass of the absorber, β is the ratio of the particle's momentum to energy, T_{max} is the maximum transfer energy from the charged particle to an electron in the medium, I^2 is the mean excitation energy of the medium, $\frac{\delta(\beta\gamma)}{2}$ is a correction factor based on the polarization of the material, and γ^2 is the lorentz factor $\frac{1}{\sqrt{1-\beta^2}}$

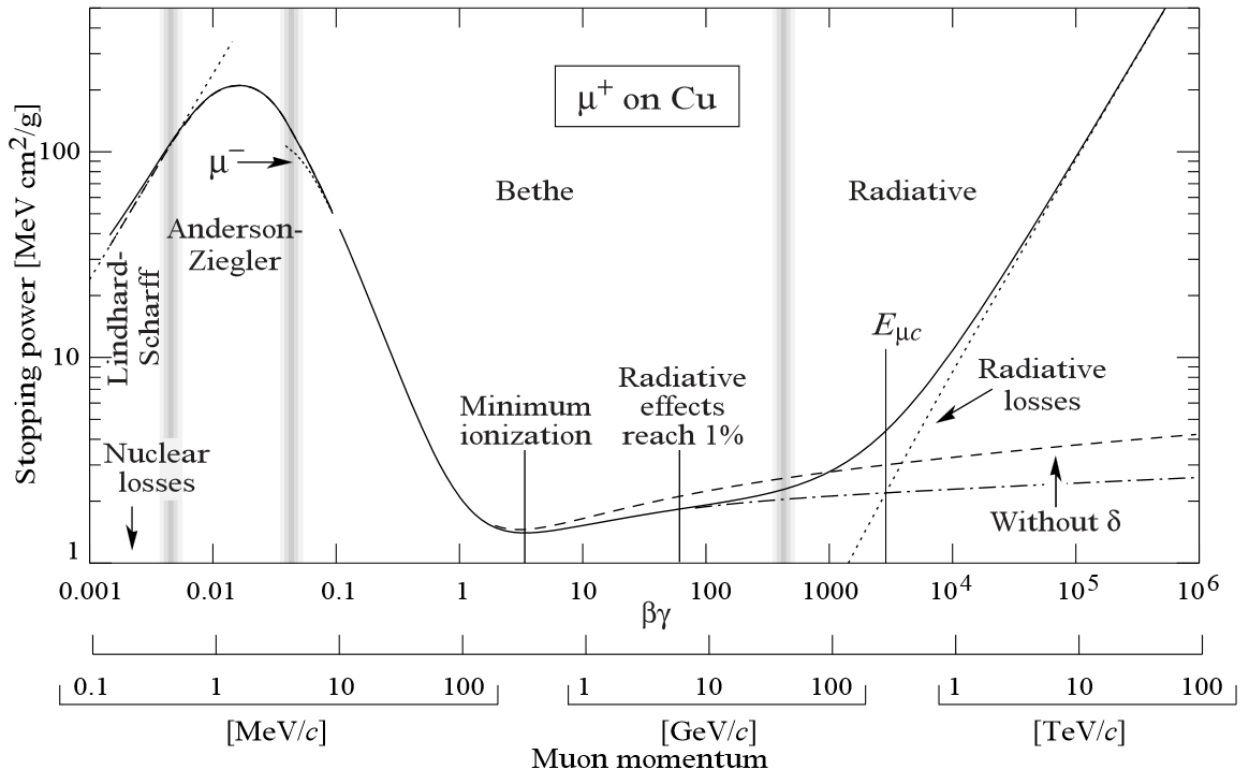


Figure 15: Energy loss of a muon traversing a copper medium between 0.1 MeV to 100 TeV [1].

Figure 15 shows the Bethe-Bloch curve for a muon over a wide kinematic range. At low energies the dominate form of energy loss is via elastic scattering, while at high energies

radiation becomes the dominate energy loss mechanism. When $\beta\gamma \approx 3$ the muon losses the least amount of energy possible and is called a minimum ionization particle(MIP).

The ALICE ITS and TPC³ cannot directly measure the energy loss of a particle traversing either sub-detector. Instead they perform PID by measuring the relative amplitudes from the sub-detectors read-out elements, pixels in the ITS and copper pads in the TPC. The amplitudes are then fit to the Bethe-Bloch equation as seen in Figure 16. Electrons weakly obey the Bethe-Bloch relationship in the kinematic ranges sensitive to the ITS and TPC and thus have a constant energy loss in both detectors.

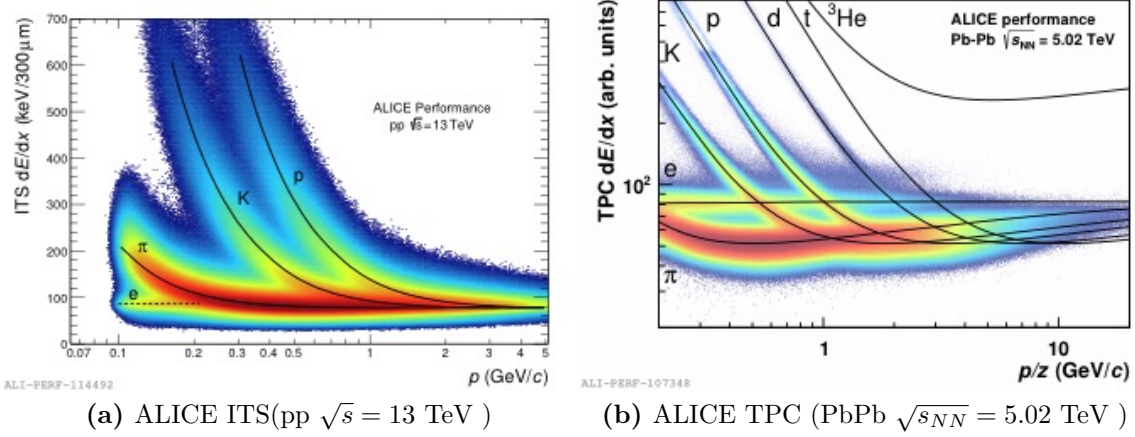


Figure 16: Specific energy loss for the ITS(*left*) and the TPC(*right*) with Bethe-Bloch fits from different particle species traversing each detector[47].

Figure 16 also shows that the Bethe-Bloch curves merge above some kinematic range, 4 GeV in the ITS and 10 GeV in the TPC. Above this kinematic range particles cannot be distinguished on a track-by-track basis, but by using statistical methods and Gaussian fits PID can be extended up to 20 GeV[48].

³See Section ?? and Section ??

Vita